RESEARCH ARTICLE

Draft tube discharge fluctuation during self-sustained pressure surge: fluorescent particle image velocimetry in two-phase flow

A. Müller · M. Dreyer · N. Andreini · F. Avellan

Abstract Hydraulic machines play an increasingly important role in providing a secondary energy reserve for the integration of renewable energy sources in the existing power grid. This requires a significant extension of their usual operating range, involving the presence of cavitating flow regimes in the draft tube. At overload conditions, the self-sustained oscillation of a large cavity at the runner outlet, called vortex rope, generates violent periodic pressure pulsations. In an effort to better understand the nature of this unstable behavior and its interaction with the surrounding hydraulic and mechanical system, the flow leaving the runner is investigated by means of particle image velocimetry. The measurements are performed in the draft tube cone of a reduced scale model of a Francis turbine. A cost-effective method for the in-house production of fluorescent seeding material is developed and described, based on off-the-shelf polyamide particles and Rhodamine B dye. Velocity profiles are obtained at three streamwise positions in the draft tube cone, and the corresponding discharge variation in presence of the vortex rope is calculated. The results suggest that 5–10 % of the discharge in the draft tube cone is passing inside the vortex rope.

A. Müller (✉) · M. Dreyer · F. Avellan
Laboratory for Hydraulic Machines, Ecole Polytechnique
Fédérale de Lausanne, Av. de Cour 33 bis, 1007 Lausanne,
Switzerland
e-mail: andres.mueller@epfl.ch

N. Andreini
Environmental Hydraulics Laboratory, Ecole Polytechnique
Fédérale de Lausanne, Station 18, 1015 Lausanne, Switzerland

1 Introduction

Cavitation occurs in various forms and locations throughout hydraulic systems and represents a major challenge to operating efficiency, safety and component lifetime (Young 1989). In hydraulic reaction turbines, the swirling flow exiting the runner in off-design operating conditions gives rise to a cavitating vortex rope. Its interaction with the surrounding flow may lead to critical instabilities in a phenomenon often referred to as pressure surge (Rheingans 1940). At overload, when the discharge is higher than the value at the best efficiency point of the turbine, called BEP, the oscillation of the vortex rope is characterized by its self-sustained nature. The resulting pressure oscillations reach a non-negligible part of the specific energy of a given operating point and thus significantly jeopardize the stability of the machine and the connected electrical power system. Such off-design operating points are increasingly required in order to ensure the smooth integration of certain inherently unsteady renewable energy sources into the existing electrical grid. The stability of hydroelectric power plants needs therefore to be completely and accurately assessed by means of reliable models. A major challenge in existing one-dimensional approaches is the modeling of the two-phase flow in the draft tube. The corresponding key parameters were introduced and characterized by several authors, where the contributions of Rubin (1966), Brennen and Acosta (1976), Brennen (1978) and Tsujimoto et al. (1997) have to be mentioned. Today, the calculation of these parameters, such as the cavitation compliance and the mass excitation source for self-oscillations, is mostly based on numerical flow simulations. In order to validate and further develop the existing computational and hydroacoustic models, the properties of this instability and its interaction with the surrounding hydraulic and mechanical

system have to be determined. The evolution of the flow field in the draft tube cone during the oscillation of the vortex rope plays a key role in this effort. However, detailed experimental investigations of the flow parameters in a test case featuring the components and the geometry of an actual power plant have been missing up to this point. If the presence of cavitation and the somewhat tricky optical access privileged almost exclusively the ex situ approach in the past, the local behavior of the flow velocity is investigated in the present study by means of particle image velocimetry (PIV). Horizontal profiles of the axial velocity component are obtained in regular time steps during the pressure oscillation, offering the possibility of following the discharge time history at several streamwise positions along the draft tube cone. The characteristic wall pressure signal is chosen as a periodic time reference. The two-phase nature of the flow required the use of fluorescent seeding material in order to eliminate the contribution of the light sheet's reflection on the cavity interface and isolate the illuminated particles. Due to the important water volume of about 30 m^3 in the test rig and the high cost of fluorescent polymer particles available on the market, a cost-effective in-house production technique is developed, based on off-the-shelf polyamide particles. The Rhodamine B dye used in the process described in Sect. 3 has ideal optical properties for the use with standard long pass filters for the PIV cameras, since it emits orange light at a wavelength centered around 600 nm. The test setup with the reduced scale model and the components of the PIV system is explained in the same section, as well as the measurement procedure and the data processing. The

significant concentration of bubbles in the flow during the preceding phase of the repetitive vortex rope collapse compromises the quality of the measurements, which requires the validation of the obtained cross-correlation maps. The resulting velocity profiles are presented in Sect. 4 for three different streamwise locations in the draft tube cone, at six uniformly distributed time steps over one period of the vortex rope oscillation. The time history of the discharge is presented at the same streamwise locations. These results are then discussed in Sect. 5 together with some critical aspects about the methods they are obtained with, before closing the article with some concluding remarks and perspectives in Sect. 6.

2 Background

Figure 1 shows a high-speed visualization of the oscillating vortex rope observed at the runner exit during full load or overload pressure surge. A LED back light source is used in order to enhance the contrast between the gaseous and the liquid phase. The six uniformly distributed snapshots over one period of the pressure oscillation show the different stages of the vortex rope formation and collapse, the latter in the presence of a significant amount of bubbles in the surrounding flow.

The mass balance in the draft tube cone during this self-sustained oscillation of the vortex rope has to be established in order to identify the mass excitation source. A control volume containing the oscillating vortex rope can be defined for this purpose, as illustrated in Fig. 2. The

Fig. 1 Oscillation of the vortex rope in the draft tube cone. The time $t = 0$ corresponds to the *peak* in the wall pressure signal and hence to the minimum volume. The instants $t = 0.17$ T, $t = 0.33$ T and $t = 0.50$ T show the growing vortex rope, whereas the pictures at $t = 0.67$ T and $t = 0.83$ T are taken during its collapse. The time steps are uniformly distributed over one period T of the pressure oscillation, separated by 93.5 ms
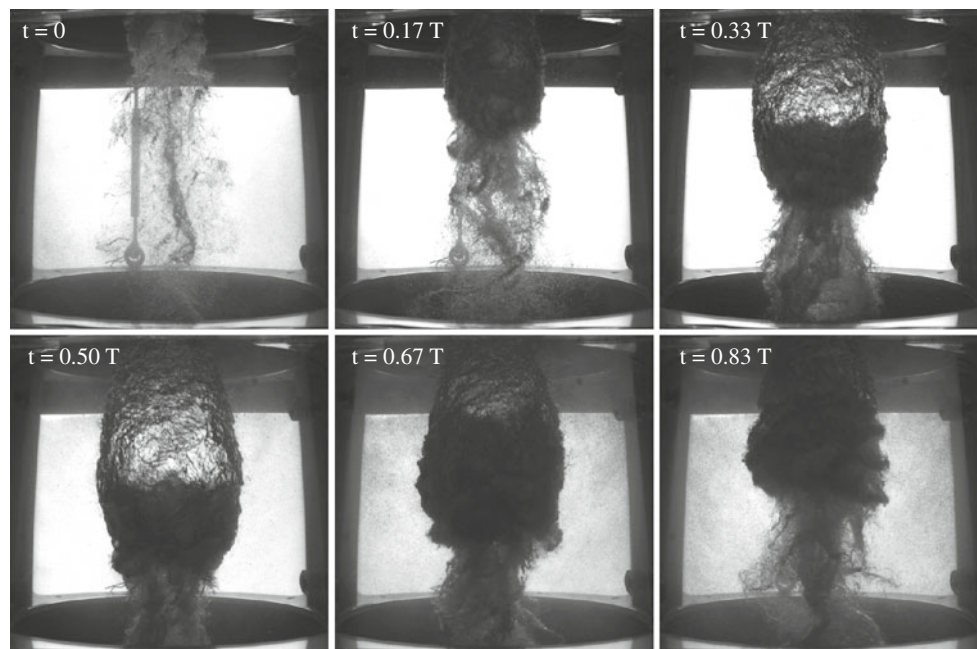
volumetric discharge through the two cross sections up- and downstream the vortex rope is represented by Q_1 and Q_2, respectively. The volume balance yields

$$Q_2 - Q_1 = \frac{\mathrm{d}V_c}{\mathrm{d}t}, \qquad (1)$$

where V_c is the cavity volume. Several authors have addressed the behavior of Q_1 and Q_2 in recent 1-D models of the draft tube flow as well as their role played in the onset of the instability (Alligné et al. 2010; Yonezawa et al. 2012; Chen et al. 2008). The timewise evolution of the discharge in the control volume, for instance at the three presently investigated axial locations A, B and C,
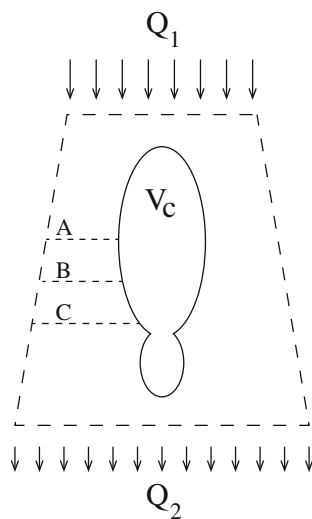
Fig. 2 Control volume in the draft tube, limited by *dashed lines*, containing a cavity of volume V_c

may point toward the respective physical properties of Q_1 and Q_2.

3 Methodology

3.1 Experimental setup

The measurements are carried out at the test facilities of the EPFL Laboratory for Hydraulic Machines on a reduced scale physical model of a Francis turbine. The real generating unit, featuring a rated power of 444 MW, is located in a power plant in British Columbia, Canada, and experiences serious overload pressure surge. A complete 1:16 reduced scale model as shown in Fig. 3 with a specific speed of $\nu = 0.27$ is manufactured, including the upstream inlet pipe, the spiral case, the runner and the draft tube consisting of the cone, the elbow and the diffuser. A generator connected to the model runner regulates the rotating speed. The test rig is operated in a closed loop configuration driven by two axial double-volute pumps. The operating conditions for the PIV measurements are characterized by a discharge coefficient of $Q_{ED} = Q/(D^2 \times \sqrt{E}) = 0.278$ and a speed coefficient of $n_{ED} = n \times D/\sqrt{E} = 0.275$, defined according to IEC standards (1999), where Q represents the discharge (m^{3}s^{-1}), D the runner outlet diameter (m), E the specific hydraulic energy (J kg^{-1}) and n the runner rotating frequency (Hz). The discharge ratio with respect to the best efficiency point is $Q/Q_{BEP} = 1.19$. Table 1 displays the characteristics of the generating unit and the reduced scale model.

The target area for the PIV is situated in a centered meridional plane of the Plexiglas draft tube cone below the
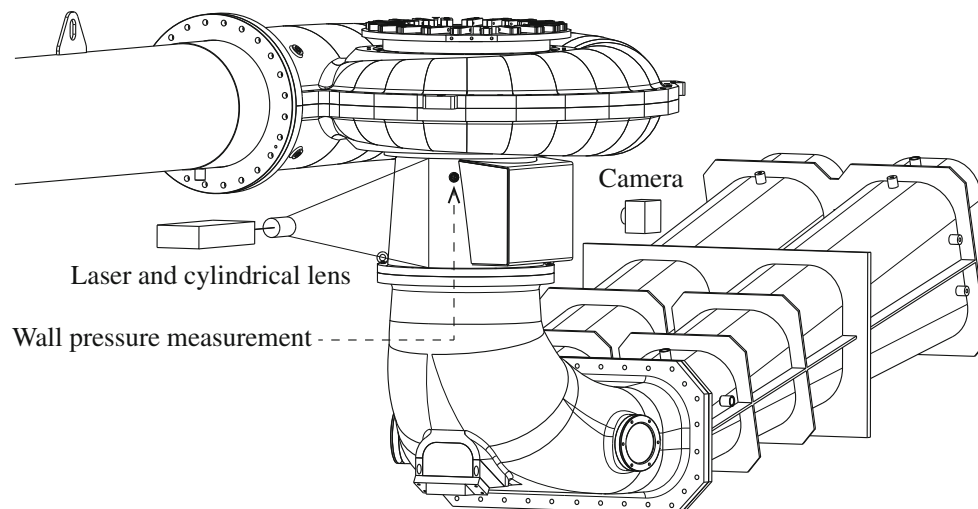
Fig. 3 Reduced scale model of the Francis turbine on the test rig. The laser is installed parallel to the inlet pipe. The camera is mounted 90° from the laser in order to view the target area through the water box window

runner outlet. The inner surface of the cone has a diameter of 0.35 m at the inlet and 0.41 m at the outlet, is 0.39 m high and has 0.04 m thick walls. In order to minimize the optical distortion due to the conical shape, a water box window is installed between the camera and the target area. The data acquisition is explained in Fig. 4. The wall pressure signal is used as a reference for an external trigger and is measured $0.3 \times D$ downstream the runner exit, with D defining the runner outlet diameter. This position is based on the experience gained from a former investigation on the same reduced scale model. The synchronization with the velocity measurements is ensured via a timing unit. The characteristics of the laser and the camera of the PIV system are summarized in Table 2.

3.2 Measurement procedure

The PIV measurements are triggered externally by the wall pressure. The corresponding TTL signal that is used by the

timing box is generated by the oscilloscope at a certain voltage level of each falling edge of the pressure signal, as illustrated in Fig. 5. The characteristic pressure peaks are due to the collapse of the vortex rope. The entire instability is investigated in several steps by defining different trigger delay values in the PIV acquisition program with respect to the generated TTL signal. For the presented case, one period of the pressure oscillation is divided into 45 sub-cycles, delimited by 46 measurement points. At each of these 46 measurement points, identified by a specific trigger delay value, 40 pairs of images are taken, each with a time of 100 μs between the individual pulses. Hence, in order to complete one measurement point, at least 40 cycles of the pressure oscillation are required. At the chosen operating conditions and a thickness of the light sheet between 2 and 3 mm, the majority of the particles remain well in the measurement plane during the time between two pulses.

3.3 Fluorescent seeding particles

Fluorescent seeding particles may be obtained from off-the-shelf 20 μm polyamide particles by the following procedure. Approximately 100 g of polyamide particles is mixed with 1 l of water and 5 g of Rhodamine B dye in a lockable glass container. The container is placed in a heated incubator at 60 °C for 1 month, during which the solution is regularly agitated in order to ensure its homogeneity. The particles have the tendency to separate from the liquid phase and float on the surface.

Table 1 Prototype and reduced scale model characteristics

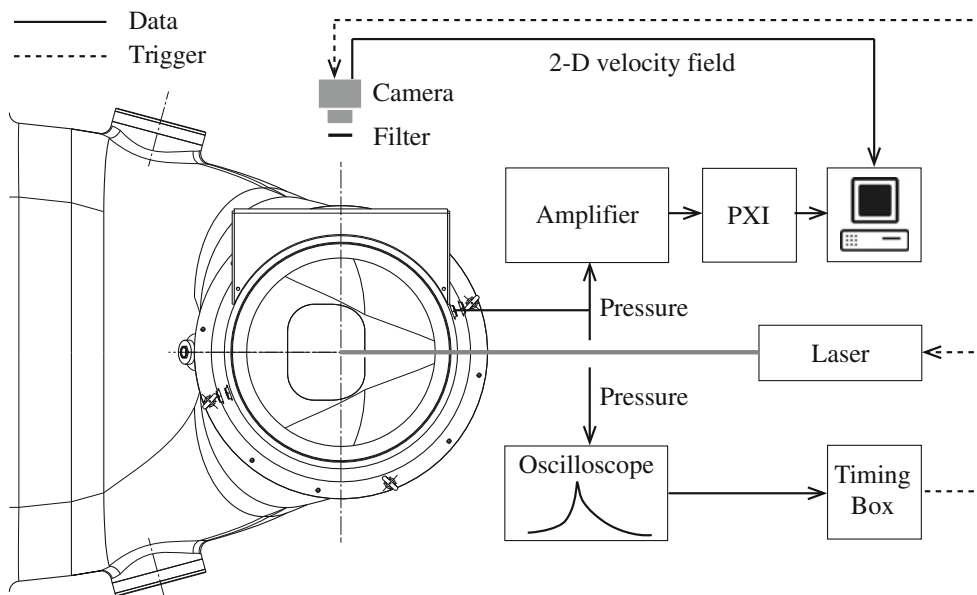|	Prototype	Model
Rated power (P)	443.7 MW	35.8 kW
Rated head (H)	170.7 m	11.7 m
Rated discharge (Q)	288 m³/s	0.366 m³/s
Runner diameter (D)	5.6 m	0.350 m
Runner speed (n)	133.3 min^{-1}	505.0 min^{-1}
Reynolds number (Re)	1.6×10^8	5.6×10^6

Fig. 4 Schematic representation of the data acquisition chain. The drawing is a horizontal cut of the draft tube cone at the axial position of the pressure sensor

Table 2 Characteristics of the PIV system

Laser	
Wavelength	532 nm
Energy	<32.5 mJ
Beam diameter	3.5 mm
Type	Frequency doubled Q-switched Nd:YAG
Model	New Wave Minilase III-15
Camera	
Resolution	2,048 × 2,048 pixels
Pixel size	7.4 μm
Lens	24 mm
Filter	Long pass (>570 nm)
Model	Dantec FlowSense EO 4M
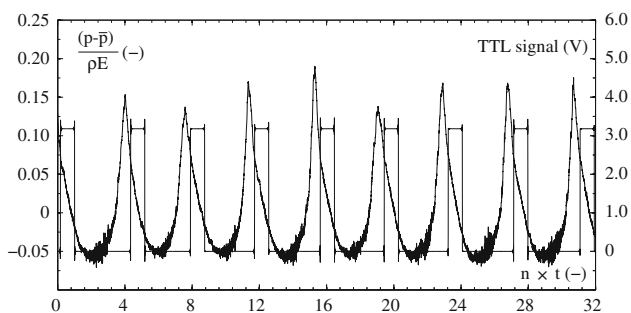
Fig. 5 Wall pressure oscillations normalized by the water density and the specific energy of the operating point as a function of the number of runner revolutions. The square TTL signal from the oscilloscope is used as the reference for the trigger output to the PIV system

Fig. 6 Büchner funnel for the filtering of the particles in a Rhodamine B solution with glass flask, rubber seal and a *funnel-shaped* ceramic cylinder with a perforated plate

Then, the particles are extracted by filtering the solution on a Büchner funnel, represented in Fig. 6. It consists of a glass flask, a vacuum tight rubber seal and 4–12 μm filter papers on the perforated plate of a funnel-shaped ceramic cylinder. The side arm of the glass flask is connected to a vacuum pump. Firstly, the solution with the particles from the incubator is further diluted with water in a suitably large glass container. The Rhodamine B solution with the particles is then poured into the funnel. The water traverses the perforated plate, drawn in by the vacuum in the glass flask, leaving the particles in form of a compressed powder on the filter paper. Once all the particles are on the filter paper, fresh water can be added several times to the funnel, where the color of the water dripping into the flask is observed. When the draining water becomes translucent, the particles can be scraped off and decanted into another glass container. There, they are diluted in ethanol or methanol in order to wash off the remaining Rhodamine B molecules which did not diffuse into the polyamide particles and are still stuck at the particles surface. After the funnel is cleaned and the filter paper is changed, the alcohol solution containing the particles is poured into the
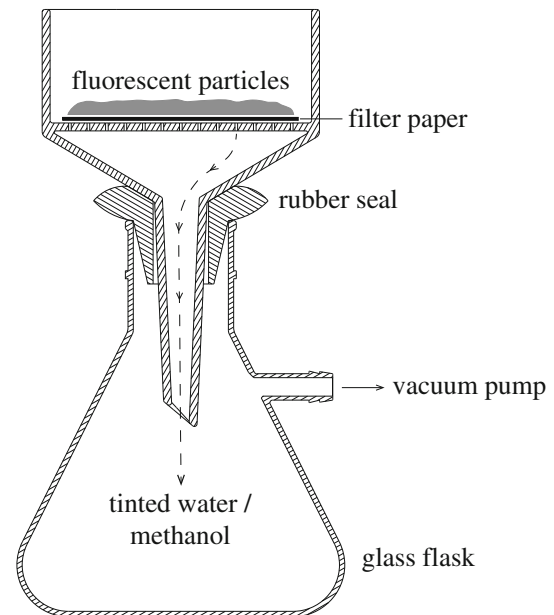
funnel. Finally, fresh water is added once more in order to verify that the water dripping into the flask is perfectly transparent. The particles are then scraped from the filter paper and stored until used. Optionally, they can be placed in the incubator for one more night to dry. Rhodamine B can cause serious damage to the eyes, skin and respiratory ways. It is therefore recommended to wear protection gloves, safety goggles and dusk masks during the entire process and to work in a well-ventilated area.

An alternative procedure to obtain inexpensive fluorescent seeding material was recently introduced by Pedocchi et al. (2008); however, this method was slightly more complicated to implement in our facilities. Moreover, the use of standard polyamide particles carries the advantage that the desired particle size is obtained easily and accurately, within a known tolerance stated by the manufacturer.

A sufficient seeding density is achieved with 1.5–2 g of particles/m^3 of water, injected into the flow in an upstream inlet pipe of the test rig, on the pressure side of the turbine.

3.4 Velocity field measurements

The images from the camera at a given measurement point are dewarped based on a calibration, taken before the actual measurements with a 200 × 200 mm dotted target disk attached to the runner nose in the Plexiglas cone. Cross-correlations between 32 × 32 pixel sized windows with a 50 % overlap are then calculated for each of the 40 image pairs and an averaging produces the mean velocity

field. This is repeated at each of the 46 measurement points. As mentioned, the presence of bubbles in the flow required a validation of the cross-correlation maps before calculating the mean vector field. This includes a range validation, where all velocity vectors with a module larger than $10 \, \mathrm{m} \times \mathrm{s}^{-1}$ are discarded. The range validation is followed by a moving average validation, where a velocity vector is compared to the average value in a surrounding field of 3×3 vectors and substituted by interpolation if the deviation exceeds 10 %. This is illustrated in Fig. 7 for $t = 0.83 \, T$, where a high concentration of bubbles is observed prior to the vortex rope collapse. In the other phases of the oscillation, the moving range validation has almost no effect on the velocity profiles.

3.5 Vortex rope edge detection

The reflections of the light sheet at the cavity interface are visible even through the long pass filter, as can be observed in Fig. 8. The vortex rope edge can therefore be detected by numerically processing the images taken by the PIV equipment. The pictures are transformed into a binary form with a threshold value determined according to the method described by Otsu (1979). As illustrated in Fig. 8, this leaves white seeding particles on a black background. In the picture row corresponding to the investigated streamwise position in the draft tube cone, the white pixels are then counted in windows of 1×16 pixels, starting from the left border of the image and moving to the right, with an overlap of 50 %. At the first iteration

where the window contains exclusively white pixels, the edge of the vortex rope is set to the left end of the given window. This is done for the first take of each of the 40 image pairs recorded at a given measurement point. The resulting mean value is then used in the calculation of the local discharge by truncating the velocity component profiles accordingly. The results from the detection algorithm were visually verified and showed a good agreement with the position of the vortex rope edge observed by the naked eye. The number of images where no valid edge was detected is only significant in the bubbly phase of the vortex rope collapse. Figure 8 also shows the three streamwise positions A, B and C used in the following investigations, axially separated by 50 mm each. Only the left side of the cavity is illuminated in the experiment. However, for the discharge calculation, it is assumed that the vortex rope is axisymmetric, based on the visualization presented in Sect. 2 The six images in Fig. 8 match the snapshots in Fig. 1 by taking the mean period T observed in the wall pressure signal as a reference.

3.6 Discharge computation

For the calculation of the discharge, the velocity profiles are limited between the vortex rope edge as detected by the described algorithm and the inner cone wall, whose position is known from the draft tube geometry. The velocity value at the vortex rope interface is obtained by linear extrapolation based on the last two valid data points outside the vortex rope. The volumetric discharge Q through a

Fig. 7 Instantaneous velocity vector field before (*top*) and after (*bottom*) moving average validation at $t = 0.83 \, T$
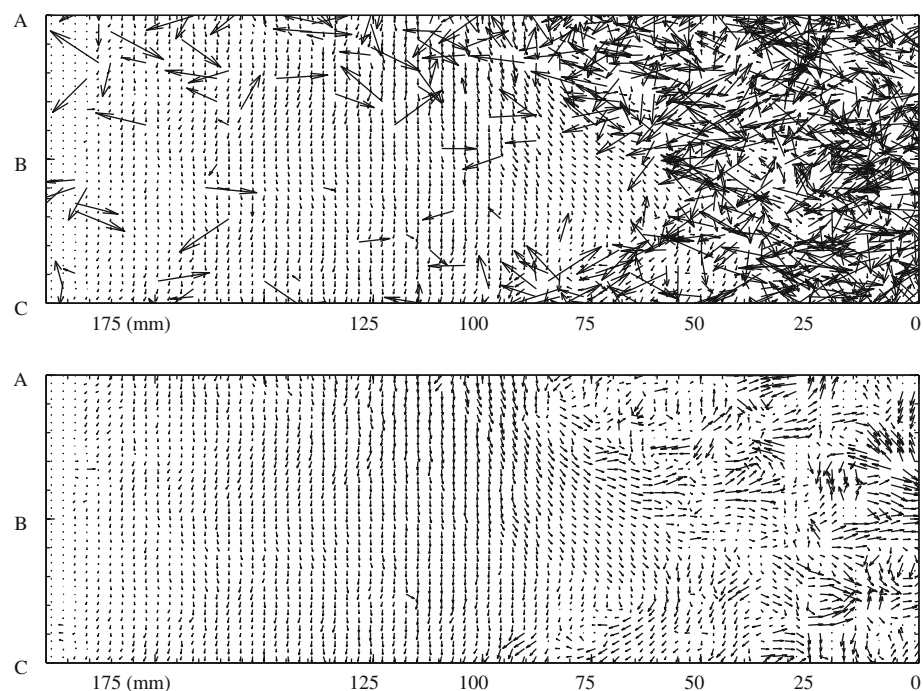
Fig. 8 Draft tube flow with fluorescent particles recorded with the PIV system. The *pictures* are uniformly distributed over one period of the pressure oscillation. The three positions A, B and C for the discharge calculation are indicated by the *horizontal dashed arrow lines*. The cone centerline is marked by the *vertical dash-dotted line*
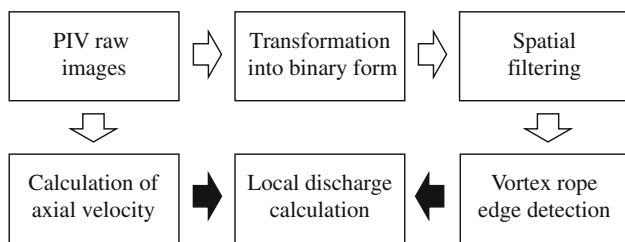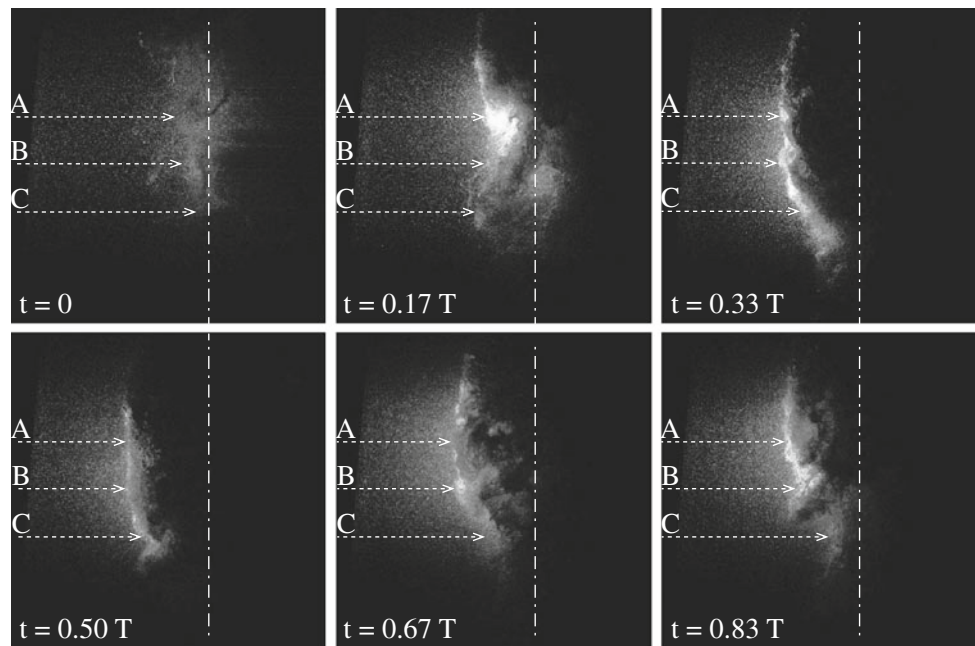

Fig. 9 Process of the discharge calculation based on the PIV measurement data. The images from the camera are used to calculate the velocity components and to detect the edge of the vortex rope

given cross section of the cone in presence of an axisymmetric, perfectly centered vortex rope is given by

$$Q = \int_{R_{\mathrm{edge}}}^{R_{\mathrm{wall}}} \int_{0}^{2\pi} C_m \times r \mathrm{d}r \mathrm{d}\theta = 2\pi \int_{R_{\mathrm{edge}}}^{R_{\mathrm{wall}}} C_m \times r \mathrm{d}r, \qquad (2)$$

where R_{edge} and R_{wall} denote the radius of the vortex rope edge and the inner cone wall, and C_m the axial velocity component. The numerical integration is performed according to the Simpson's rule. The overall process of the discharge calculation based on the PIV measurement data and the edge detection algorithm is explained by the diagram in Fig. 9.

4 Results

4.1 Velocity profiles

In the images from the high-speed camera and the PIV system, it is observed that the concentration of bubbles,

most likely originating from the cavitation on the runner blades, rises in the flow during the phase of the collapse of the vortex rope. This compromises the quality of the PIV measurements, requiring the use of the previously mentioned validation techniques. Furthermore, the reflections of the laser on the vortex rope illuminates the border regions and hence particles which are not necessarily located in the original measurement plane. Consequently, several data points may exist beyond the observed limit of the vortex rope edge. Figures 10 and 11 show the velocity profiles (upper curves) at the streamwise position B, corresponding to the snapshots in Figs. 1 and 8, together with the standard deviation (lower curves). The maximum value on the R axis corresponds to the position of the inner draft tube cone wall and hence to the radius of the given cross section, while the position of the vortex rope edge as computed from the PIV images is illustrated by the vertical dashed line. The origin of the R axis represents the cone centerline.

It is observed that for the bubbly phases of the collapse, corresponding to Figs. 10a and 11c, a considerable number of velocity vectors were replaced in the validation process. Finally, the velocity profiles at the same six instants, based on the validated data, are presented in Fig. 12 for the three streamwise positions A, B and C.

4.2 Vortex rope edge detection

The periodic time history of the vortex rope radius, as calculated by the algorithm described in Sect. 3.5, is presented in Fig. 13 for the streamwise positions A, B and C. It is observed that the values for positions A and B are
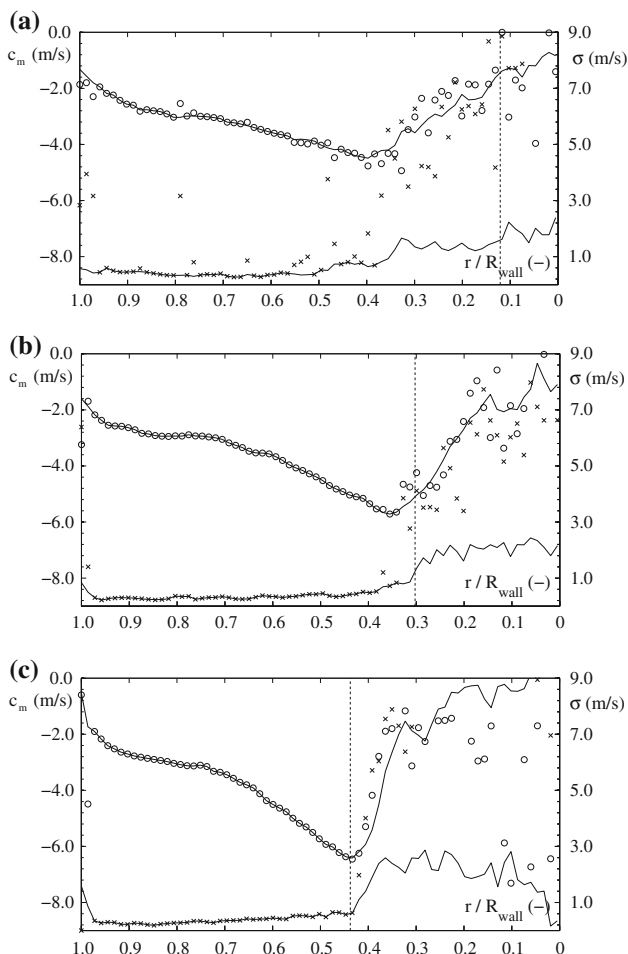
Fig. 10 Raw averaged axial velocity components C_m (*open circle*) and corresponding standard deviation values σ (*times symbol*) together with validated data (*continuous lines*) for $t = 0$–$t = 0.33\ T$ plotted against the cone radius R at the streamwise position B. The origin of the R axis corresponds to the position of the cone centerline and its maximum to the inner cone wall. The *dashed line* represents the edge of the vortex rope as computed by the described algorithm. **a** $t = 0$. **b** $t = 0.17\ T$. **c** $t = 0.33\ T$

Fig. 11 The same as Fig. 10 for $t = 0.50\ T$–$t = 0.83\ T$. **a** $t = 0.50\ T$. **b** $t = 0.67\ T$. **c** $t = 0.83\ T$

similar and that the mean radius at position C, situated at the lower end of the main body of the vortex rope, is significantly smaller.

4.3 Discharge

Based on the generated velocity profiles and Eq. (2), the discharge can be calculated at each of the 46 measurement points distributed over one period T of the pressure oscillation. Figure 14 shows the resulting curves at the streamwise positions A, B and C. The discharge values are made non-dimensional with the mean value Q_{OP} measured in an upstream inlet pipe by an electromagnetic flow meter.
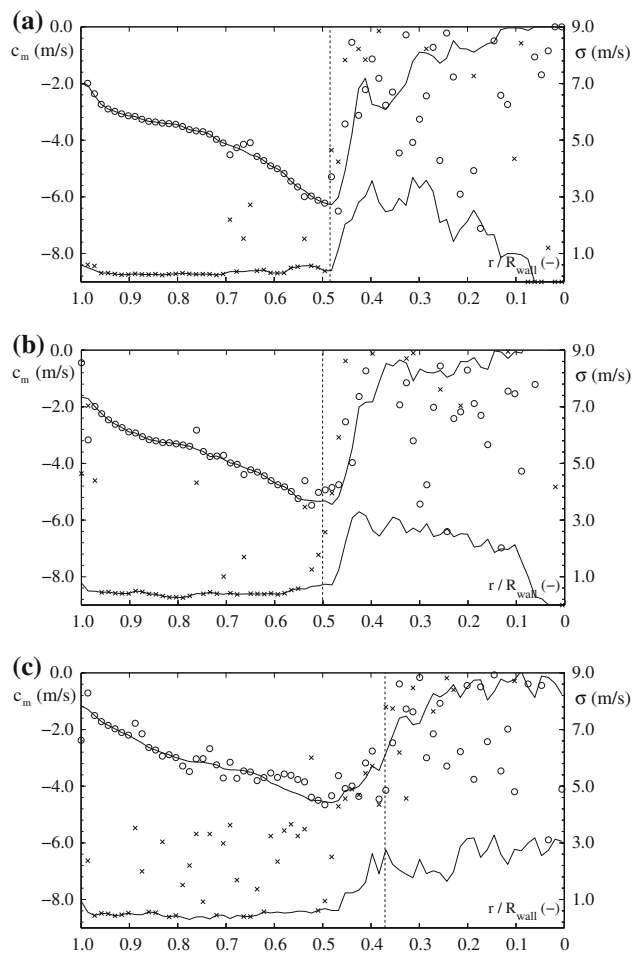
5 Discussion

5.1 Methodology

Even if the nature of the wall pressure signal in Fig. 5 is fairly regular, small variations between the different cycles naturally occur. This implies that the flow configuration at a given pressure level, which serves as the reference for the trigger output, does not remain constant over the 40 measurements taken at that point. This variation has an impact on the calculated discharge by altering the relevant flow surface via the detected vortex rope edge position. This is illustrated in Fig. 15, where the maximum and minimum discharge values are obtained by including the standard deviation of the mean vortex rope position in the discharge calculation at each of the 46 measurement points.

The accuracy of the vortex rope detection varies significantly over the whole period. The developed algorithm is a simplified first approach with the tendency to slightly underestimate the rope radius and hence overestimate the
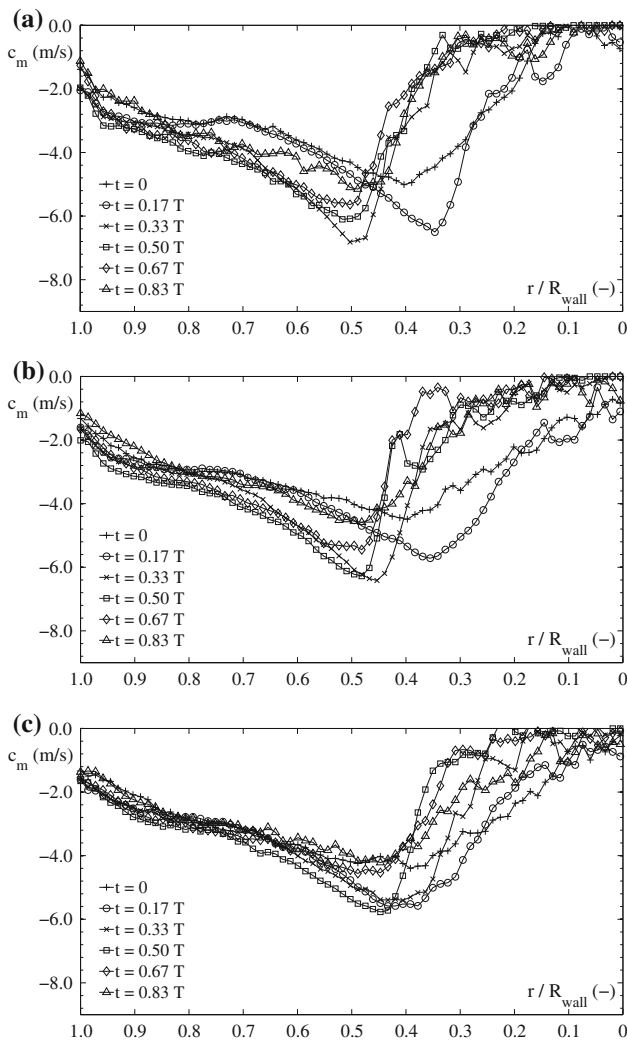
Fig. 12 Validated averaged axial velocity components C_m plotted against the cone radius R at six uniformly distributed time steps over one period of the pressure oscillation for the streamwise positions A, B and C. The origin of the R axis corresponds to the position of the cone centerline and its maximum to the inner cone wall. **a** Position A, **b** position B, **c** position C
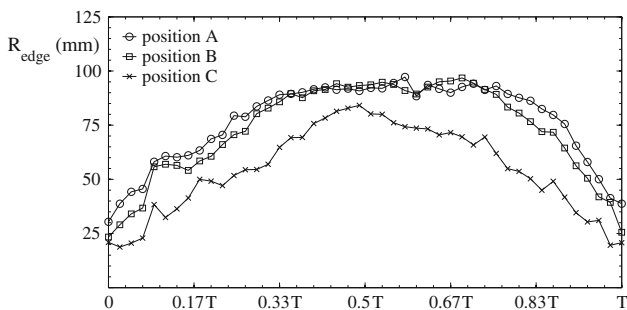

Fig. 13 Vortex rope radius plotted against the time during on period of the pressure oscillation at the streamwise positions A, B and C
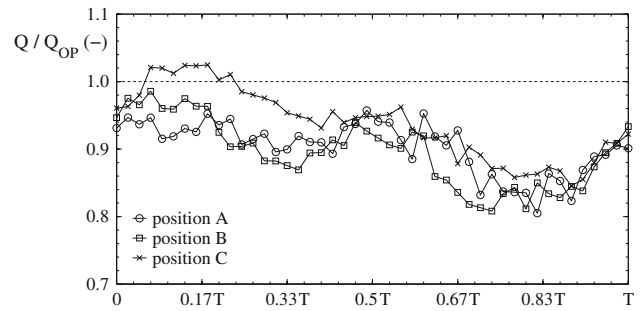

Fig. 14 Discharge time history at the streamwise positions A, B and C during one period of the pressure oscillation made non-dimensional with the mean discharge Q_{OP} in the test rig
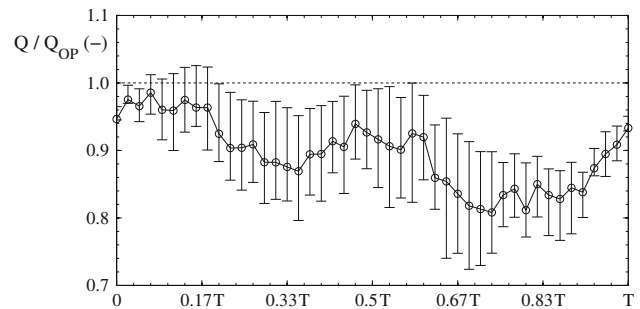

Fig. 15 Discharge time history (*open circle*) at the streamwise position B during one period of the pressure oscillation made non-dimensional with the mean discharge Q_{OP} in the test rig. Only the standard deviation of the position of the vortex rope edge is considered in the error calculation

discharge in the growing phase of the cavity and more significantly underestimate the discharge in the bubbly phase of its collapse. Furthermore, as it can also be read from Figs. 10a and 11c, the quality of the measurements is increasingly compromised with the appearance of the bubbles descending from the runner blades, and a large number of velocity measurements are substituted in the validation process. It is expected that a seeding density higher than the presently observed 7–9 particles per interrogation window of 32×32 pixels would generally increase the overall accuracy of the measurements by lowering the uncertainty in the cross-correlation calculation, as suggested by Willert and Gharib (1991). Furthermore, the use of a slightly more powerful laser device would enlarge the target area and facilitate the image processing.

5.2 Fluorescent seeding particles

The obtained seeding material was well suited for the presented test case. The initial amount introduced in the

test rig was used over a period of 5 days, without a noticeable decrease in the intensity of the scattered light. A more detailed study of the optical properties as a function of the relevant parameters involved in the fabrication process is being established and shall be the subject of a later publication.

5.3 Velocity and discharge time history

Figure 12 shows that the velocity range, over which the six profiles covering one period of the pressure oscillation vary, is decreasing in an increasing axial direction. If this implicates a decreasing variation of the discharge in the same direction cannot be clearly read from Fig. 14; the agreement of this observation with models, which feature a more significant variation of Q_2 compared to the variation of Q_1 in Eq. (1) at overload conditions (Alligné et al. 2010; Yonezawa et al. 2012) has to be further discussed. The mean values of Q_A, Q_B and Q_C show that the discharge is significantly underestimated by 9.7, 10.5 and 6.25 %, respectively, suggesting a partial flow though the vortex rope. An interesting observation in this regard is the change in transparency of certain parts of the vortex rope, visible for instance at $t = 0.33\ T$, $t = 0.50\ T$ and $t = 0.67\ T$ of Fig. 1, which may indicate a variation of its vapor content.

In view of the missing portion of the discharge, one might be tempted to evaluate the data points beyond the observed limit of the vortex rope. The corresponding measurements in the vicinity of the liquid–vapor interface feature, however, a higher level of uncertainty due to the light sheet reflection, as already described by Lawson et al. (1999) in the case of a large collapsing bubble. It is therefore doubtful that the illuminated particles are situated in the original measurement plane and that their validation makes physical sense.

6 Conclusions and perspectives

PIV measurements were performed in a draft tube of a reduced scale Francis turbine model in the presence of an oscillating vortex rope. A procedure to obtain fluorescent seeding material from off-the-shelf polyamide particles and Rhodamine B dye is introduced and described. The evolution of the axial flow velocity field is investigated by defining 46 measurement points over one period of the pressure oscillation. The concentration of bubbles in the draft tube flow increases during the collapse of the vortex rope and compromises the accuracy of the velocity measurements, which is compensated by applying range and moving average validation techniques to the obtained cross-correlation maps. The position of the vortex rope edge is determined by detecting the reflection of the light

sheet at the gaseous interface in the PIV images by means of a spatial filter. The velocity profiles are presented for six time steps uniformly distributed over one period T of the pressure oscillation, at three different streamwise positions. The corresponding time history of the discharge is calculated at the same streamwise positions with a resolution of $1/46\ T$. It is observed that the axial velocity components vary less over the pressure oscillation period T with an increasing downstream position. The mean values of the discharge suggest a proportion of 5–10 % of the flow being discharged through the vortex rope. The main source of inaccuracy in the discharge calculation is the detection of the vortex rope edge, which has to be refined and adapted to the different phases of the oscillation. The results remain, however, valid as a first quantitative study of the discharge behavior in the draft tube during full load pressure surge.

The obtained results are currently being used to compare the measured flow field in the draft tube to results obtained with unsteady two-phase CFD. One-dimensional stability models will consequently benefit from this validation process, since their key parameters are based on such numerical flow simulations. The behavior of the discharge may in the future be compared to simultaneously recorded quantities, such as the torque on the runner shaft, the instantaneous runner speed or pressure fluctuations throughout the circuit in order to gain a global view of the instability and its exchange with the system.

References

Alligné S, Maruzewski P, Dinh T, Wang B, Fedorov A, Iosfin J, Avellan F (2010) Prediction of a Francis turbine prototype full load instability from investigations on the reduced scale model. IOP Conf Ser Earth Environ Sci 12(1):012025

Brennen C (1978) Bubbly flow model for the dynamic characteristics of cavitating pumps. J Fluid Mech 89(pt 2):223–240

Brennen C, Acosta A (1976) Dynamic transfer function for a cavitating inducer. J Fluids Eng Transa ASME Ser 98 1(2):182–191

Chen C, Nicolet C, Yonezawa K, Farhat M, Avellan F, Tsujimoto Y (2008) One-dimensional analysis of full load draft tube surge. J Fluids Eng Trans ASME 130(4):0411061–0411066

IEC Standards (1999) 60193: hydraulic turbines, storage pumps and pump–turbines—model acceptance tests. International Electrotechnic Commission, 2nd edn

Lawson N, Guerre A, Liow JL, Rudman M (1999) Experimental and numerical comparisons of the break-up of a large bubble. Exp Fluids 26(6):524–534

Otsu N (1979) Threshold selection method from gray-level histograms. IEEE Trans Syst Man Cybern SMC 9(1):62–66

Pedocchi F, Martin J, Garca M (2008) Inexpensive fluorescent particles for large-scale experiments using particle image velocimetry. Exp Fluids 45(1):183

Rheingans W (1940) Power swings in hydroelectric power plants. Trans ASME 62:171–184

Rubin S (1966) Longitudinal instability of liquid rockets due to propulsion feedback/POGO/. J Spacecr Rocket 3:1188–1195

Tsujimoto Y, Yoshida Y, Maekawa Y, Watanabe S, Hashimoto T (1997) Observations of oscillating cavitation of an inducer. J Fluids Eng Trans ASME 119(4):775–781

Willert C, Gharib M (1991) Digital particle image velocimetry. Exp Fluids 10(4):181–193

Yonezawa K, Konishi D, Miyagawa K, Avellan F, Doerfler P, Tsujimoto Y (2012) Cavitation surge in a small model test facility simulating a hydraulic power plant. Int J Fluid Mach Syst 5(4):152–160

Young F (1989) Cavitation. McGraw-Hill Book Company, London